

## Article

# On the Donor: Acceptor Features for Poly(3-hexylthiophene): TiO<sub>2</sub> Quantum Dots Hybrid Materials Obtained via Water Vapor Flow Assisted Sol-Gel Growth

Dominique Mombrú, Mariano Romero \* , Ricardo Faccio \*  and Alvaro W. Mombrú \*

Centro NanoMat & Área Física, Departamento de Experimentación y Teoría de la Estructura de la Materia y sus Aplicaciones (DETEMA), Facultad de Química, Universidad de la República, Montevideo C.P. 11800, Uruguay

\* Correspondence: mromero@fq.edu.uy (M.R.); rfaccio@fq.edu.uy (R.F.); amombru@fq.edu.uy (A.W.M.)

**Abstract:** Here, we present a novel methodology for the preparation of P3HT:TiO<sub>2</sub> quantum dots hybrid materials via water vapor flow-assisted sol-gel growth focusing on the structural, optical and electrical property characterization complemented with first-principles calculations as a promising donor–acceptor system for polymer and hybrid solar cells. X-ray diffraction and UV-Vis spectroscopy analyses suggest that the increasing concentration of TiO<sub>2</sub> quantum dots leads to the formation of higher amounts of amorphous regions while the crystalline regions exhibited interesting aspect ratio modifications for the P3HT polymer. Raman spectra evidenced the formation of charge carriers in the P3HT with increasing TiO<sub>2</sub> quantum dots content and the P3HT:TiO<sub>2</sub> 50:50 weight ratio resulted in the best composition for optimizing the bulk electronic conductivity, as evidenced by impedance spectroscopy studies. Our DFT calculations performed for a simplified model of the P3HT:TiO<sub>2</sub> interface revealed that there is an important contribution of the thiophene carbon atoms states in the conduction band at the Fermi level. Finally, our DFT calculations also reveal an evident gain of electron density at the TiO<sub>2</sub> (101) surface while the thiophene rings showed a loss of the electron density, thus confirming that the P3HT:TiO<sub>2</sub> junction acts as a good donor–acceptor system. In our opinion, these results not only present a novel methodology for the preparation of P3HT:TiO<sub>2</sub> quantum dots hybrid materials but also reveal some key aspects to guide the more rational design of polymer and hybrid solar cells.

**Keywords:** poly(3-hexylthiophene); TiO<sub>2</sub> quantum dots; sol-gel; hybrid materials; donor–acceptor; DFT calculations



**Citation:** Mombrú, D.; Romero, M.; Faccio, R.; Mombrú, A.W. On the Donor: Acceptor Features for Poly(3-hexylthiophene): TiO<sub>2</sub> Quantum Dots Hybrid Materials Obtained via Water Vapor Flow Assisted Sol-Gel Growth. *Polymers* **2023**, *15*, 1706. <https://doi.org/10.3390/polym15071706>

Academic Editor: Barbara Simončič

Received: 23 February 2023

Revised: 23 March 2023

Accepted: 26 March 2023

Published: 29 March 2023



**Copyright:** © 2023 by the authors. Licensee MDPI, Basel, Switzerland. This article is an open access article distributed under the terms and conditions of the Creative Commons Attribution (CC BY) license (<https://creativecommons.org/licenses/by/4.0/>).

## 1. Introduction

Recently, there is a growing interest in the preparation of donor–acceptor polymer composites triggered by their use in active layers materials for polymer solar cells [1–3]. While the donor material is typically a semiconducting polymer such as thiophene-based conjugated polymers, one of the most popular acceptor materials is [6,6]-phenyl-(C71 or C61)-butyric acid methyl ester (PC61BM or PC71BM) fullerene [4,5]. These fullerene-derived acceptor materials are well known for their high electron affinity and mobility, but also, low absorption in the visible spectra and a high cost of fabrication, making them nonideal candidates for technological applications. For this reason, in the past few years, non-fullerene acceptors have been studied to obtain higher light absorption and lower costs of fabrication [6–10]. In the search for non-fullerene acceptors, important breakthroughs and recent progress have been achieved in the development of polymer donor–polymer acceptor (all-polymer) bulk heterojunction solar cells [11]. However, hybrid metal oxide–polymer solar cells also represent an emerging technology that holds the advantage of pronounced difference in dielectric constants of electron donor and acceptor compounds, controllable phase separation, and chemical stability compared to conventional organic photovoltaic [12]. The preparation of polymer solar cells based on poly(3-hexylthiophene)

(P3HT) donor using inorganic nanoparticles acceptors such as the low-cost and nontoxic titanium oxide ( $\text{TiO}_2$ ) has been already reported [13–15]. Other more recent approaches for P3HT: $\text{TiO}_2$  donor–acceptor materials with  $\text{TiO}_2$  in the form of a mesoporous matrix have been reported to yield slightly higher power conversion efficiency values [16]. The use of small molecules and oligomers as modifiers for P3HT: $\text{TiO}_2$  hybrid solar cells has also been recently explored yielding an enhancement in their performances [17–19]. However, up to now, only a few studies have been reported on fundamental aspects of P3HT: $\text{TiO}_2$  hybrid materials for solar cell applications, and thus we have poor information to rationally improve their performances. For instance, Leijtens et al. have shown that the mobility of the materials is heavily dependent on the charge carrier density as well as the morphology employing transient absorption spectroscopy combined with time-resolved photo-conductivity measurements [20]. Frischknecht et al. have shown that P3HT: $\text{TiO}_2$  hybrid solar cells present a relevant dependence of the photocurrent on the incident light wavelength, exhibiting a particularly strong photocurrent enhancement upon UV monochromatic illumination due to the filling of shallow traps that become donor sites with an n-doping effect improving the titania electron mobilities [21]. It has been demonstrated that the use of time-of-flight (TOF) measurements are quite appropriate for observing the effects of the molecular structures, trap states, scattering centers, and dispersivity on hole/electron carrier transport [22–26]. In one of the later reports, bulk heterojunctions are studied in thick ( $>1 \mu\text{m}$ ) devices showing that electron transport occurs mainly by diffusion in the bulk of the active layer [24]. In addition, other TOF measurement studies have shown highly unbalanced transport for which the hole transport shows trap-free behavior while the electron transport heavily shows trap-limited behavior [26]. However, to the best of our knowledge, there is still a lack of insights into and correlations between the structural, optical and electrical properties of these hybrid materials considering the semi-crystalline nature of P3HT coexisting with the crystalline  $\text{TiO}_2$  nanostructures. For instance, in most studies reported in the literature, hybrid polymer–inorganic nanocomposites are treated as a biphasic system and typically the P3HT polymer phase is treated as full crystalline or full amorphous, and no structural nor physical chemistry in-depth characterization of the material is provided. There are almost no reports studying these systems, particularly their electronic properties related to their donor–acceptor interface from a first-principles approach probably due to their large computational cost. In this manuscript, we present a novel methodology for the preparation of P3HT: $\text{TiO}_2$  quantum dots hybrid materials via water vapor flow-assisted sol-gel growth. In addition, we focus on the structural, optical and electrical properties characterization complemented with first-principles calculations revealing some key aspects of their donor–acceptor interactions that can be very useful to guide the more rational design of polymer and hybrid solar cells among other applications.

## 2. Materials and Methods

### 2.1. Experimental Section

The preparation of P3HT: $\text{TiO}_2$  nanocomposites was based on the sol-gel synthesis via water vapor flow diffusion, as it was previously reported for other polymers [27–29]. In total, 0.3 g of regioregular poly(3-hexylthiophene-2,5-diyl) (P3HT) polymer, purchased from Sigma-Aldrich with a  $M_w$  of 50,000–100,000 and a regioregularity above 90%, were suspended in 50 mL of tetrahydrofuran (THF) and kept stirred at  $T = 70 \text{ }^\circ\text{C}$ . Then, 1 mL of deionized water was added slowly dropwise. The corresponding amount of titanium tetrapropoxide (TTP) was added to the P3HT suspension and kept stirred at  $T = 70 \text{ }^\circ\text{C}$  until dryness. The resulting powder was exposed to deionized water vapor at  $T = 80 \text{ }^\circ\text{C}$  with a vapor flow of  $\sim 1 \text{ mL/min}$  for 16 h. All samples were dried at  $T = 70 \text{ }^\circ\text{C}$  under vacuum for 7 h in order to eliminate residual water and propanol generated from the hydrolysis process. Finally, the samples were pressed in the form of pellets with a  $1.2 \text{ cm}^2$  diameter and a 0.1 cm thickness. The samples that corresponded to 30%, 50% and 70% of the weight fraction of  $\text{TiO}_2$  quantum dots were named  $\times 30$ ,  $\times 50$  and  $\times 70$ , respectively.

## 2.2. Characterization of Samples

X-ray diffraction powder (XRD) was performed using a Rigaku Ultima IV diffractometer with  $\text{CuK}\alpha$  radiation in a Bragg–Brentano configuration, in the  $2\theta = 2.00\text{--}80.00^\circ$  range, using steps of  $0.02^\circ$ , with 10 s integration time per step. MicroRaman imaging and corresponding spectra for all samples were collected using WITec Alpha 300-RA equipment, working with an excitation laser of 785 nm wavelength and the laser power below  $\sim 10$  mW to avoid polymer decomposition. Solid-state UV-Vis reflectance measurements were performed utilizing a UV-vis spectrophotometer Shimadzu UV-2600 with an integrating sphere in the 1400–220 nm range. The AC impedance spectroscopy analysis was performed using a Gamry Reference 3000 impedance analyzer with the deposition of silver electrodes on both sides of the samples. The applied AC voltage amplitude was 100 mV in the 0.1 Hz–1 MHz frequency range with applied DC voltages in the  $V_{\text{DC}} = 0\text{--}3$  V range using a 0.5 V step.

## 2.3. Computational Section

The computational calculations were performed using Density Functional Theory (DFT) [30,31] using the VASP code (Vienna ab initio simulation package) [32–35]. Pseudopotentials were applied with a plane-wave basis set with a projector augmented wave (PAW) method [36,37] using a generalized gradient approximation (GGA) as the exchange–correlation function according to Perdew–Burke–Ernzerhof (PBE) [38]. The employed pseudopotentials correspond to the following configurations:  $3s^2 3p^6 3d^2 4s^2$  for titanium,  $3s^2 3p^4$  for sulfur,  $2s^2 2p^4$  for oxygen,  $2s^2 2p^2$  for carbon and  $1s^1$  for hydrogen atoms. A  $4 \times 4 \times 1$  k-point mesh was set for the full Brillouin Zone (vacuum space along c-axis), a 400 eV energy cutoff was utilized to expand the Kohn–Sham orbitals into plane wave basis sets, and dipole corrections were applied along the direction perpendicular to the surface. The structures were then optimized until the forces in all the atoms were lower than a  $0.01 \text{ eV}/\text{\AA}$  tolerance value. We simulated the adsorption of poly(3-hexylthiophene-2,5-diyl) (P3HT) on  $\text{TiO}_2$  anatase (101) surface after the previous optimization of isolated counterparts. We used a 3-hexylthiophene trimer, named 3M, with the composition  $\text{C}_{15}\text{S}_3\text{H}_{14}$  (as a simplified model of P3HT) and a slab model of anatase  $\text{TiO}_2$  (101) as it is the most favorable surface in terms of surface energy [39] consisting of a unit cell with  $a = 10.5 \text{ \AA}$ ,  $b = 14.9 \text{ \AA}$  and  $c = 25.2 \text{ \AA}$ , having a vacuum space of  $\sim 15 \text{ \AA}$  aligned along the c-axis. After achieving the optimization of the isolated 3M molecule and  $\text{TiO}_2$  surface, we proceeded to optimize the 3M adsorption on  $\text{TiO}_2$  anatase (101) surface, allowing all the atomic positions to relax and optimize to obtain the joint donor–acceptor system named 3M: $\text{TiO}_2$ .

## 3. Results

X-ray diffraction patterns collected for  $\times 30$ ,  $\times 50$  and  $\times 70$  samples are shown in Figure 1a. Typical XRD profiles for  $\text{TiO}_2$  anatase quantum dots are present in all XRD measurements with broad peaks at  $2\theta = 25.4, 38.1, 47.9, 54.6, 62.8, 69.4$  and  $75.3^\circ$ , assigned as (101), (103)(004)(112), (200), (105)(211), (213)(204), (116)(220) and (215)(301) planes, respectively [40]. Typical diffraction peaks corresponding to P3HT polymer are detected at  $2\theta \sim 5.6^\circ, 10.8^\circ$  and  $16.5^\circ$  ascribed with (100), (200) and (300) Miller planes, assigned with a monoclinic structure with a  $\text{P}2_1/c$  space group [41,42]. A broad diffraction peak associated with the amorphous region of P3HT is observed at  $2\theta \sim 20^\circ$  according to both experimental and theoretical studies reported in the literature [42–46].

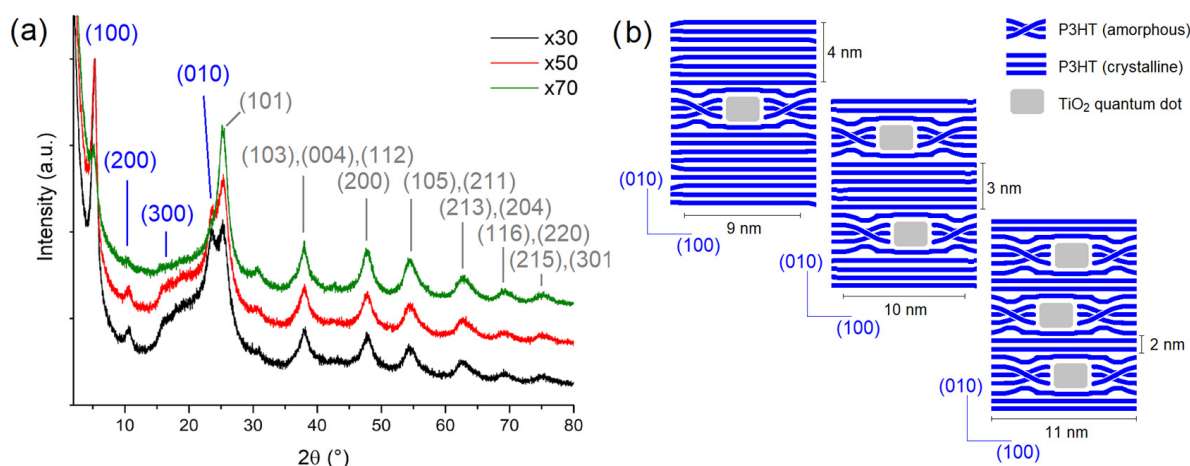


**Figure 1.** (a) X-ray diffraction patterns and (b) schematization of most relevant structural features for  $\times 30$ ,  $\times 50$  and  $\times 70$  nanocomposites.

However, particularly  $\times 30$  and  $\times 50$  samples exhibit a well-defined crystalline peak at  $2\theta \sim 23.6^\circ$ , which is associated with the (010) plane of the P3HT crystalline region [42–46].

As expected, those peaks associated with P3HT become less notorious when the amount of TiO<sub>2</sub> is higher, becoming practically undetectable for the sample of  $\times 70$ . To make a quantitative approach, we use the Bragg equation to estimate the most relevant d-spacing distances and we use the Scherrer equation to estimate the most relevant crystalline domain sizes. For this purpose, we perform a Lorentzian deconvolution of selected diffraction peaks; i.e., the (101) plane for TiO<sub>2</sub> in its anatase polymorph and the (100) and (010) planes for P3HT crystalline regions, as depicted in Figure S1. First, no drastic shifting was evidenced for the d-spacing for the (101) plane for TiO<sub>2</sub> from  $d = 0.351$  nm nor for the mean crystallite size from  $D = 4.7$ – $5.2$  nm for all compositions. Then, the (100) plane for P3HT associated with the in-plane thiophene-to-thiophene distances showed an increase in its corresponding d-spacing from  $d = 1.66$  to  $1.70$  nm with increasing TiO<sub>2</sub>-QDs concentration from  $\times 30$  to  $\times 70$ . However, the (010) plane for P3HT associated with the out-of-plane thiophene-to-thiophene distances showed no drastic modifications of its corresponding d-spacing  $d = 0.377$  nm with increasing TiO<sub>2</sub>-QDs concentration. Interestingly, we evidenced that the mean crystallite sizes associated with (100) and (010) planes for P3HT crystalline regions exhibited opposite trends with increasing TiO<sub>2</sub> quantum dots content. The P3HT mean crystallite size showed an increment from  $9.5$  to  $11.1$  nm considering the (100) plane but a decrease from  $4.1$  to  $2.2$  nm considering the (010) plane with increasing TiO<sub>2</sub>-QDs concentration from  $\times 30$  to  $\times 70$ , as schematized in Figure 1b. MicroRaman imaging for  $\times 30$ ,  $\times 50$  and  $\times 70$  nanocomposites are shown in Figure 2. P3HT-rich and TiO<sub>2</sub>-rich regions were defined using the characteristic vibrational modes of P3HT (C=C mode,  $\sim 1450$  cm<sup>-1</sup>) and TiO<sub>2</sub> (E<sub>g</sub> mode,  $\sim 140$  cm<sup>-1</sup>), colored in blue and white, respectively.

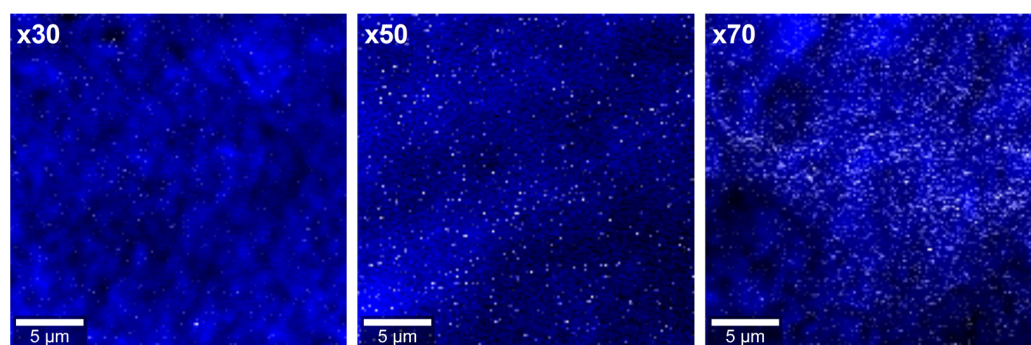


**Figure 2.** microRaman imaging for  $\times 30$ ,  $\times 50$  and  $\times 70$  nanocomposites.

Excellent homogeneity and no drastic segregation were observed for all cases, as evidenced in Figure 2. The averaged microRaman spectra for  $\times 30$ ,  $\times 50$  and  $\times 70$  nanocomposites are shown in Figure 3a and all of them presented peaks at  $1380\text{ cm}^{-1}$  ascribed to the C–C intra-ring stretching mode and  $1450\text{ cm}^{-1}$  ascribed to the C=C bond stretching associated with thiophene rings of the P3HT [47]. In the case of  $\times 50$  and  $\times 70$  samples, a shoulder peak emerges at approximately  $1430\text{ cm}^{-1}$ , which could be associated with the formation of charge carriers in the thiophene rings of P3HT [48,49]. The UV-Vis spectra for  $\times 30$ ,  $\times 50$  and  $\times 70$  nanocomposites collected in the reflectance configuration are shown in Figure 3b. According to the literature, crystalline P3HT presented a characteristic peak at  $\sim 600\text{--}750\text{ nm}$ , ascribed to the  $\pi\text{--}\pi^*$  electronic transitions through P3HT chains [50]. It has been already evidenced that highly ordered single crystals of P3HT composed of closely packed  $\pi\text{--}\pi$  stacked fully extended chains exhibit a UV-Vis absorption peak with a maximum at  $\sim 670\text{ nm}$  [51]. On the other hand, the P3HT solution spectrum only exhibits a single broad UV-Vis absorption peak at  $\sim 455\text{ nm}$ , mainly related to intra-chain states of individual P3HT chains in a flexible random-coil conformation [51]. The P3HT in the solid state with different levels of crystallinity and disorder is usually observed as a sum of both contributions [51]. In our case, we observe a broad peak at  $\sim 600\text{--}750\text{ nm}$  associated with crystalline regions of P3HT and a peak at  $\sim 450\text{ nm}$  associated with larger amounts of amorphous regions in the P3HT [46]. Interestingly, there is a blue shift of the  $\sim 600\text{--}750\text{ nm}$  peak and a red shift of the  $\sim 450\text{ nm}$  peak when the amounts of  $\text{TiO}_2$  increase, i.e.,  $\times 50$  and  $\times 70$ , and these shifts are notorious in comparison with isolated P3HT as observed in our previous work [46]. This could suggest that  $\text{TiO}_2$  quantum dots in the composite leads to the reduction in crystalline regions at the expense of the formation of amorphous regions in the polymer [51,52]. Impedance spectra obtained with  $100\text{ mV}$  AC amplitude and zero applied DC bias for  $\times 30$ ,  $\times 50$  and  $\times 70$  are shown in Figure 4a. Bode plots displayed as phase versus frequency plots are shown in the upper panel of Figure 4a and Nyquist plots represented as imaginary ( $-Z''$ ) versus real impedance ( $Z'$ ) are shown in the lower panel of Figure 4a. Both Nyquist and Bode plots were best fitted with the circuit model shown in the inset of Figure 4a, characterized by the series combination of two parallel combinations of a resistor (R) and constant phase element (CPE). The two contributions to the electrical transport can be attributed to different zones in the nanocomposites: one corresponding to a bulk zone ( $R_b\text{--}CPE_b$ ) and the other to a depletion zone ( $R_d\text{--}CPE_d$ ) of the polymer nanocomposites, in agreement with previous reports [28,46]. For all cases,  $R_b\text{--}CPE_b$  contribution is one order of magnitude lower than the  $R_d\text{--}CPE_d$  contribution corroborating that the depletion region is governing the whole electronic transport in the samples.

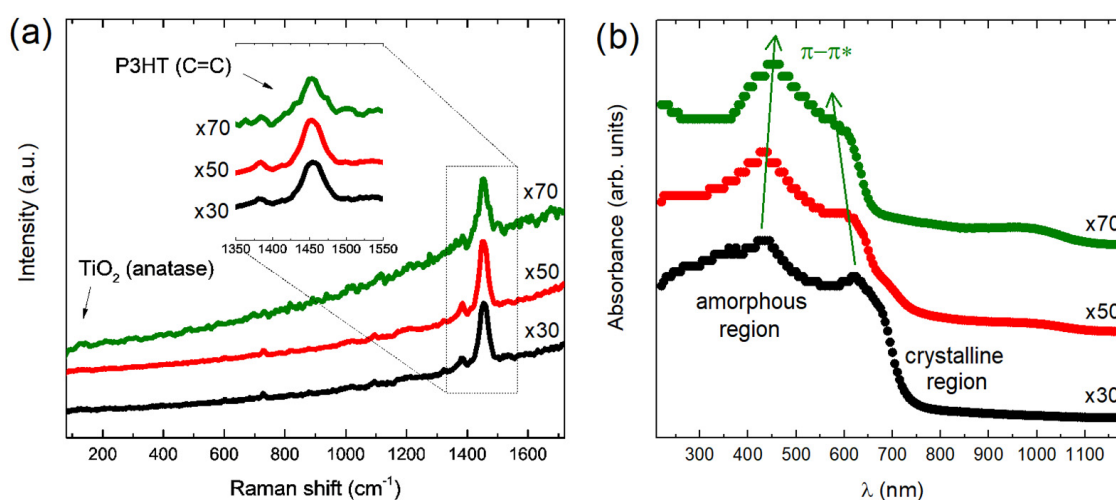


**Figure 3.** (a) microRaman spectra and (b) UV-Vis absorbance spectra collected in reflectance mode for  $\times 30$ ,  $\times 50$  and  $\times 70$  nanocomposites.

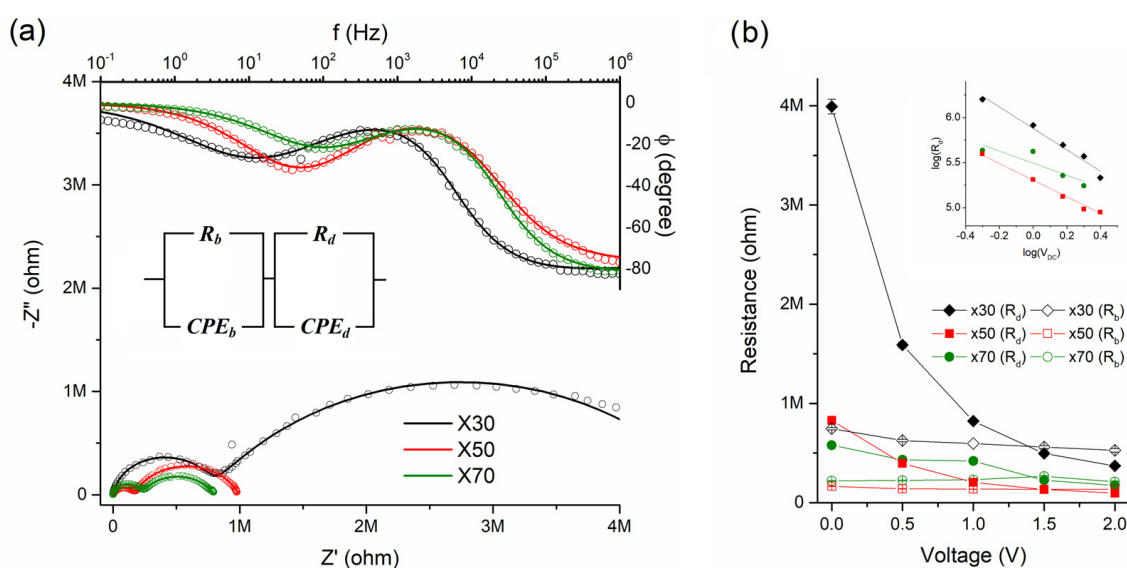


**Figure 4.** (a) Impedance spectroscopy displayed as Bode (upper panel) and Nyquist (lower panel) and (b) Bulk-region ( $R_b$ ) and depletion-region ( $R_d$ ) resistances as a function of applied dc voltage ( $V_{DC}$ ) and  $\log(R_d)$  vs.  $\log(V_{DC})$  plots (inset) for  $\times 30$ ,  $\times 50$  and  $\times 70$ .

The increasing amounts of  $\text{TiO}_2$  quantum dots lead to a drastic decrease in several orders of magnitude in the total resistance of the nanocomposites. The associated total conductivities were calculated using:

$$\sigma_T = l/A(R_b + R_d)$$

With  $l$  and  $A$  being the thickness and effective electrode area of the samples, yielding  $\sigma_T = 2.11 \times 10^{-8}$ ,  $1.00 \times 10^{-7}$  and  $1.25 \times 10^{-7} \text{ S}\cdot\text{cm}^{-1}$  for  $X = 30$ ,  $50$  and  $70$ , respectively. It is important to note that the total conductivity for P3HT has been reported to be  $\sim 3 \times 10^{-7} \text{ S}\cdot\text{cm}^{-1}$  [46] while that for  $\text{TiO}_2$ -QDs is expected to be well below  $10^{-12} \text{ S}\cdot\text{cm}^{-1}$  [53]. The P3HT: $\text{TiO}_2$  bulk conductivity can be defined considering only the bulk resistance following:

$$\sigma_b = l/A \cdot R_b$$

Yielding  $\sigma_b = 1.34 \times 10^{-7}$ ,  $6.05 \times 10^{-7}$  and  $4.53 \times 10^{-7} \text{ S}\cdot\text{cm}^{-1}$  for  $\times 30$ ,  $\times 50$  and  $\times 70$ , respectively. This is suggesting that the P3HT: $\text{TiO}_2$  50:50 weight ratio is the best composition in optimizing the bulk electronic conductivity, which is comparable to that observed for previous studies on PVK: $\text{TiO}_2$  obtained by the same preparation technique [28]. The increment of charge carriers with increasing  $\text{TiO}_2$  quantum dots concentration can be explained in terms of P3HT: $\text{TiO}_2$  donor–acceptor interactions as we will address later in the manuscript when discussing our DFT calculations results. However, the optimization of electronic conductivity for the P3HT: $\text{TiO}_2$  50:50 weight ratio can be also interpreted in terms of enhanced thiophene–thiophene interactions as a consequence of structural rearrangements of P3HT conducting chains favored somehow by this critical amount of  $\text{TiO}_2$  quantum dots yielding to an optimization of the percolation pathway of the conducting polymer phase embedded in the  $\text{TiO}_2$  insulating matrix. We also performed impedance spectroscopy at different DC voltages from 0–2 V to have more insight into both electronic transport contributions, as shown in Figure S2. Each electronic resistance contribution as a function of applied dc bias ( $V_{DC}$ ) for  $\times 30$ ,  $\times 50$  and  $\times 70$  is shown in Figure 4b. The bulk region-associated resistances ( $R_b$ ) showed a slight decrease with almost constant values while the depleted region-associated resistance ( $R_d$ ) shows a more drastic decrease with increasing DC voltage.

The larger resistance process related to the dependence of the interface-depleted region resistance ( $R_d$ ) on the applied DC voltage can be shown by the slope ( $-m$ ) in the  $\log(R_d)$

vs.  $\log(V_{DC})$  plots. The  $m$  values showed  $m \sim 1.2$ , 1.1 and 0.8 values for  $\times 30$ ,  $\times 50$  and  $\times 70$ , respectively, indicating that the charge carriers exhibit a near ohmic behavior typical of semiconductor material where carriers are generated thermally by the promotion of electrons from the valence band to the conduction band [54]. In our case, the promotion of carriers can be also favored by the presence of donor–acceptor interactions in P3HT:TiO<sub>2</sub> nanocomposites, as we will discuss later in the manuscript. In the following lines, we will discuss our DFT calculations for our simplified model for the P3HT:TiO<sub>2</sub> system. First, in order to analyze the adsorption process, the corresponding adsorption energies for all structures were calculated according to the following expression:

$$\Delta E = E_{3M:TiO_2} - [E_{TiO_2} + E_{3M}]$$

where  $E_{3M:TiO_2}$  is the 3M:TiO<sub>2</sub> total energy,  $E_{TiO_2}$  is the total energy for isolated TiO<sub>2</sub>(101) surface and  $E_{3M}$  is the isolated 3M trimer total energy. The calculated adsorption energy was  $E_{ads} = -0.109$  eV suggesting a favorable process for 3M:TiO<sub>2</sub> interaction with respect to their isolated counterparts. In order to discuss the electronic structure of the system, we compute the density of electronic states (DOS) for the 3M:TiO<sub>2</sub> system as shown in the upper panel of Figure 5. The DOS for the 3M:TiO<sub>2</sub> system presents a similarity with the typical DOS observed for the isolated TiO<sub>2</sub> (101) system, characterized by a typical n-type semiconductor behavior with a main contribution of oxygen (O-p states) and titanium (Ti-d states) for the valence and conduction band, respectively [55].

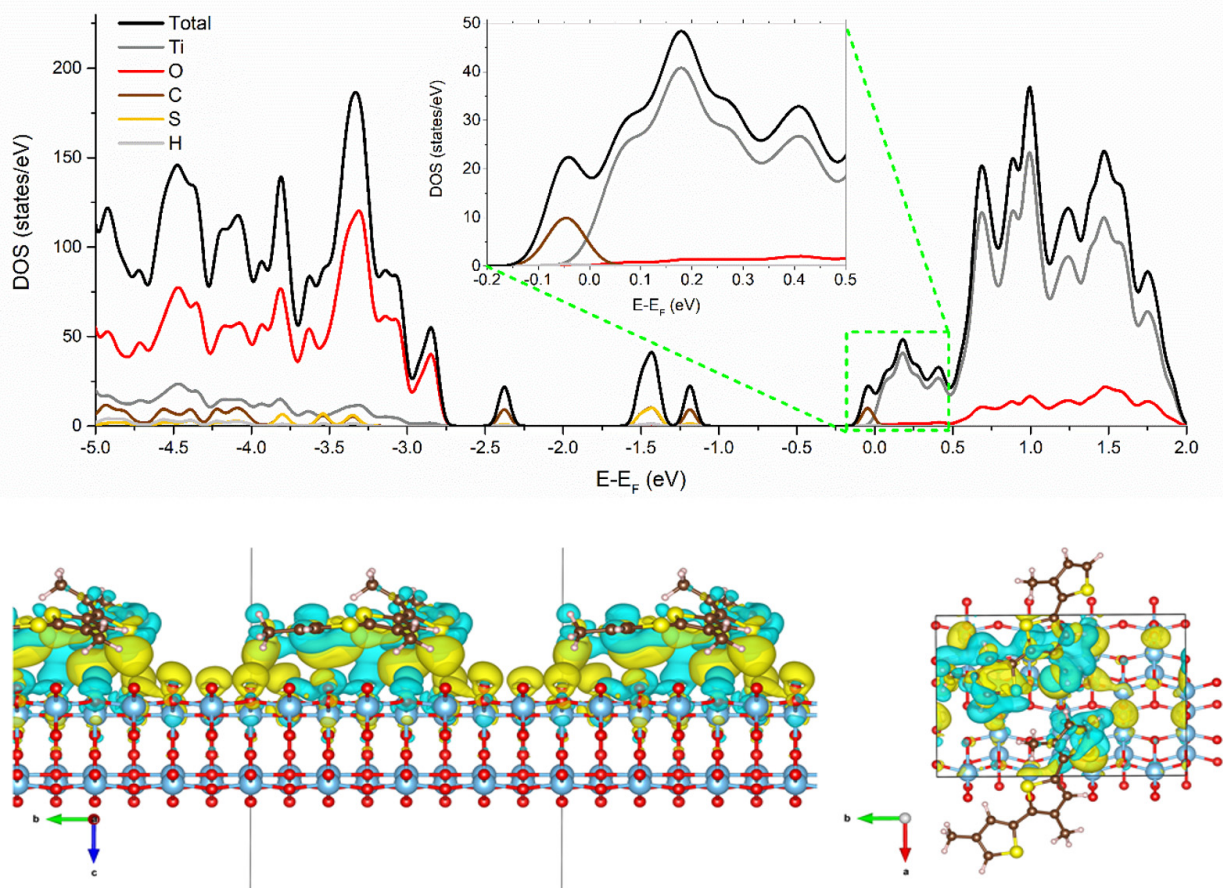


**Figure 5.** Total and projected density of states (DOS) (**upper** panel) and charge density differences (**lower** panel) for TiO<sub>2</sub>/3M system, where the loss and gain of electron density are represented in blue and yellow, respectively. References for atoms (colors) are carbon (brown), sulfur (yellow), hydrogen (light grey), oxygen (red) and titanium (dark grey).

The DOS for the 3M:TiO<sub>2</sub> system presented characteristic peaks associated with the thiophene oligomer HOMO states mostly below  $-2.5$  eV but also some peaks between  $-1.1$  and  $-1.7$  eV which are mainly associated with  $\pi$  electrons located on the thiophene rings of P3HT oligomer rather than with defect states, as already observed in the literature [56]. In addition, the DOS for the 3M:TiO<sub>2</sub> system also exhibits an important contribution of the thiophene oligomer LUMO states at the Fermi level, as depicted in the upper panel of Figure 5. This suggests that the thiophene groups are effectively donating electrons toward the TiO<sub>2</sub> (101) surface. To have more insight into this donor–acceptor interaction, we calculate the charge density difference ( $\Delta\rho$ ) using the following expression:

$$\Delta\rho(r) = \rho(r)_{3M:TiO_2} - [\rho(r)_{TiO_2} + \rho(r)_{3M}]$$

The charge density difference mapping for the 3M:TiO<sub>2</sub> system is depicted in the lower panel of Figure 5. There is an evident gain of electron density at the TiO<sub>2</sub> (101) surface, while the 3M trimer showed a loss of the electron density, thus confirming that the 3M:TiO<sub>2</sub> junction acts as a good donor–acceptor system. It is important to remark that our DFT calculations refer to a quite simplified model of the real situation in P3HT:TiO<sub>2</sub> hybrid materials. Nonetheless, it is interesting to point out that our modeling is quite useful to have insights into the P3HT:TiO<sub>2</sub> interface for TiO<sub>2</sub> quantum dots most stable surface in contact with P3HT in both amorphous and crystalline forms. This is because the portion of P3HT modeled as the 3M trimer; i.e., an “amorphous” portion of the P3HT chain, is the more probable scenario not only for amorphous P3HT but also for a defectuous grain boundary of crystalline P3HT. However, it is also important to mention that a huge number of other types of spatial configurations, partially for P3HT, can be also present in such a complex organic–inorganic interface.

#### 4. Conclusions

A novel methodology for the preparation of P3HT:TiO<sub>2</sub> quantum dots hybrid materials via water vapor flow-assisted sol-gel growth has been presented. Our particular focus on the structural, optical and electrical properties characterization revealed interesting features for their potential application in polymer and hybrid solar cells. X-ray diffraction and UV-Vis spectroscopy analyses suggest that the increasing concentration of TiO<sub>2</sub> quantum dots leads to the formation of higher amounts of amorphous regions in the P3HT polymer. Interestingly, we evidenced that the mean crystallite sizes associated with (100) and (010) planes for P3HT crystalline regions exhibited opposite trends with increasing TiO<sub>2</sub> quantum dots content. Raman spectra evidenced the formation of charge carriers in the P3HT with increasing TiO<sub>2</sub> quantum dots content. The P3HT:TiO<sub>2</sub> bulk conductivity is enhanced for the 50:50 weight ratio suggesting that this is the best composition for optimizing the bulk electronic conductivity. Our DFT calculations performed for a simplified model of the P3HT:TiO<sub>2</sub> interface revealed that there is an important contribution of the thiophene carbon atoms states in the conduction band at the Fermi level. Finally, our DFT calculations also reveal that there is an evident gain of electron density at the TiO<sub>2</sub> (101) surface while the thiophene rings showed a loss of the electron density, thus confirming that the P3HT:TiO<sub>2</sub> junction acts as a good donor–acceptor system. In our opinion, these results not only present a novel methodology for the preparation of P3HT:TiO<sub>2</sub> quantum dots hybrid materials but also reveal some key aspects to guide the more rational design of polymer and hybrid solar cells.

**Supplementary Materials:** The following supporting information can be downloaded at: <https://www.mdpi.com/article/10.3390/polym15071706/s1>, Figure S1: Selected d-spacing and mean crystalline size as a function of TiO<sub>2</sub>-QDs concentration; Figure S2: Impedance modulus (upper panel) and phase (middle panel) versus frequency, and Nyquist (lower panel) for (a)  $\times 30$ , (b)  $\times 50$  and (c)  $\times 70$  at  $V_{DC} = 0-3$  V.

**Author Contributions:** Conceptualization, M.R., R.F. and A.W.M.; investigation, D.M., M.R., R.F. and A.W.M.; writing—original draft preparation, D.M., M.R., R.F. and A.W.M.; supervision, A.W.M. All authors have read and agreed to the published version of the manuscript.

**Funding:** This research received no external funding.

**Institutional Review Board Statement:** Not applicable.

**Informed Consent Statement:** Not applicable.

**Data Availability Statement:** The data presented in this study are available on request from the corresponding author.

**Acknowledgments:** The authors wish to thank the support of Uruguayan CSIC, CAP, ANII and PEDECIBA funding institutions.

**Conflicts of Interest:** The authors declare no conflict of interest.

## References

1. Liu, W.; Li, S.; Huang, J.; Yang, S.; Chen, J.; Zuo, L.; Shi, M.; Zhan, X.; Li, C.-Z.; Chen, H. Nonfullerene Tandem Organic Solar Cells with High Open-Circuit Voltage of 1.97 V. *Adv. Mater.* **2016**, *28*, 9729–9734. [[CrossRef](#)] [[PubMed](#)]
2. Guo, W.; Zhao, B.; Xin, J.; Liu, H.; Mi, Y.; Zhang, J.; Guo, Z.; Wei, W.; Ma, W.; Gao, C.; et al. Non-Fullerene Small Molecular Acceptors Based on Dithienocyclopentafluorene and Dithienocyclopentacarbazole Cores for Polymer Solar Cells. *Dyes Pigm.* **2017**, *144*, 48–57. [[CrossRef](#)]
3. Chakravarthi, N.; Kranthiraja, K.; Gunasekar, K.; Gal, Y.-S.; Cho, Y.-R.; Jin, S.-H. Alkoxyphenyl-Thiophene, -Selenophene and -Furan Substituted Benzodithiophene Based 2d  $\pi$ -Conjugated Polymers for Polymer Solar Cells and Effect of Chalcogen on Optoelectronic Properties. *Synth. Met.* **2016**, *222*, 356–363. [[CrossRef](#)]
4. He, Y.; Li, Y. Fullerene Derivative Acceptors for High Performance Polymer Solar Cells. *Phys. Chem. Chem. Phys.* **2011**, *13*, 1970–1983. [[CrossRef](#)] [[PubMed](#)]
5. Liu, T.; Troisi, A. What Makes Fullerene Acceptors Special as Electron Acceptors in Organic Solar Cells and How to Replace Them. *Adv. Mater.* **2013**, *25*, 1038–1041. [[CrossRef](#)]
6. Anthony, J.E. Small-Molecule, Nonfullerene Acceptors for Polymer Bulk Heterojunction Organic Photovoltaics. *Chem. Mater.* **2011**, *23*, 583–590. [[CrossRef](#)]
7. Lin, Y.; Li, Y.; Zhan, X. Small Molecule Semiconductors for High-Efficiency Organic Photovoltaics. *Chem. Soc. Rev.* **2012**, *41*, 4245–4272. [[CrossRef](#)]
8. Lin, Y.; Zhan, X. Non-Fullerene Acceptors for Organic Photovoltaics: An Emerging Horizon. *Mater. Horiz.* **2014**, *1*, 470–488. [[CrossRef](#)]
9. Nielsen, C.B.; Holliday, S.; Chen, H.-Y.; Cryer, S.J.; McCulloch, I. Non-Fullerene Electron Acceptors for Use in Organic Solar Cells. *Acc. Chem. Res.* **2015**, *48*, 2803–2812. [[CrossRef](#)]
10. Lin, Y.; Zhan, X. Oligomer Molecules for Efficient Organic Photovoltaics. *Acc. Chem. Res.* **2016**, *49*, 175–183. [[CrossRef](#)]
11. Facchetti, A. Polymer donor–polymer acceptor (all-polymer) solar cells. *Mater. Today* **2013**, *16*, 123–132. [[CrossRef](#)]
12. Wright, M.; Uddin, A. Organic-inorganic hybrid solar cells: A comparative review. *Sol. Energy Mater. Sol. Cells.* **2012**, *107*, 87–111. [[CrossRef](#)]
13. Wu, M.C.; Chang, C.H.; Lo, H.H.; Lin, Y.S.; Lin, Y.Y.; Yen, W.C.; Su, W.F.; Chen, Y.F.; Chen, C.W. Nanoscale morphology and performance of molecular-weight-dependent poly (3-hexylthiophene)/TiO<sub>2</sub> nanorod hybrid solar cells. *J. Mater. Chem.* **2008**, *18*, 4097–4102. [[CrossRef](#)]
14. Lin, Y.Y.; Chu, T.H.; Li, S.S.; Chuang, C.H.; Chang, C.H.; Su, W.F.; Chang, C.P.; Chu, M.W.; Chen, C.W. Interfacial nanostructuring on the performance of polymer/TiO<sub>2</sub> nanorod bulk heterojunction solar cells. *J. Am. Chem. Soc.* **2009**, *131*, 3644–3649. [[CrossRef](#)]
15. Lee, J.; Jho, J.Y. Fabrication of highly ordered and vertically oriented TiO<sub>2</sub> nanotube arrays for ordered heterojunction polymer/inorganic hybrid solar cell. *Sol. Energy Mater. Sol. Cells.* **2011**, *95*, 3152–3156. [[CrossRef](#)]
16. Abrusci, A.; Ding, I.K.; Al-Hashimi, M.; Segal-Peretz, T.; McGehee, M.D.; Heeney, M.; Frey, G.L.; Snaith, H.J. Facile infiltration of semiconducting polymer into mesoporous electrodes for hybrid solar cells. *Energy Environ. Sci.* **2011**, *4*, 3051–3058. [[CrossRef](#)]
17. Weickert, J.; Zimmermann, E.; Reindl, J.B.; Pfadler, T.; Dorman, J.A.; Petrozza, A.; Schmidt-Mende, L. Synergistic effects of interfacial modifiers enhance current and voltage in hybrid solar cells. *APL Mater.* **2013**, *1*, 042109. [[CrossRef](#)]
18. Planells, M.; Abate, A.; Snaith, H.J.; Robertson, N. Oligothiophene Interlayer Effect on Photocurrent Generation for Hybrid TiO<sub>2</sub>/P3HT Solar Cells. *ACS Appl. Mater. Interfaces* **2014**, *6*, 17226–17235. [[CrossRef](#)]
19. Phan, H.; Jahnke, J.P.; Chmelka, B.F.; Nguyen, T.Q. Structural and optoelectronic properties of hybrid bulk-heterojunction materials based on conjugated small molecules and mesostructured TiO<sub>2</sub>. *Appl. Phys. Lett.* **2014**, *104*, 233305. [[CrossRef](#)]
20. Leijtens, T.; Lim, J.; Teuscher, J.; Park, T.; Snaith, H.J. Charge Density Dependent Mobility of Organic Hole-Transporters and Mesoporous TiO<sub>2</sub> Determined by Transient Mobility Spectroscopy: Implications to Dye-Sensitized and Organic Solar Cells. *Adv. Mater.* **2013**, *25*, 3227–3233. [[CrossRef](#)] [[PubMed](#)]

21. Frischknecht, A.K.; Yacuzzi, E.; Plá, J.; Perez, M.D. Anomalous photocurrent response of hybrid TiO<sub>2</sub>:P3HT solar cells under different incident light wavelengths. *Sol. Energy Mater. Sol. Cells* **2016**, *157*, 907–912. [[CrossRef](#)]
22. Cheung, C.H.; Tsung, K.K.; Kwok, K.C.; So, S.K. Using thin film transistors to quantify carrier transport properties of amorphous organic semiconductors. *Appl. Phys. Lett.* **2008**, *93*, 083307. [[CrossRef](#)]
23. Tsung, K.K.; So, S.K. Carrier trapping and scattering in amorphous organic hole transporter. *Appl. Phys. Lett.* **2008**, *92*, 103315. [[CrossRef](#)]
24. Morfa, A.J.; Nardes, A.M.; Shaheen, S.E.; Kopidakis, N.; van de Lagemaat, J. Time-of-Flight Studies of Electron-Collection Kinetics in Polymer: Fullerene Bulk-Heterojunction Solar Cells. *Adv. Funct. Mater.* **2011**, *21*, 2580–2586. [[CrossRef](#)]
25. Liu, S.W.; Lee, C.C.; Su, W.C.; Yuan, C.H.; Lin, C.F.; Chen, K.T.; Shu, Y.S.; Li, Y.Z.; Su, T.H.; Huang, B.Y.; et al. Downscaling the sample thickness to sub-micrometers by employing organic photovoltaic materials as a charge-generation layer in the time-of-flight measurement. *Sci. Rep.* **2015**, *5*, 10384. [[CrossRef](#)]
26. Rohloff, R.; Kotadiya, N.B.; Crăciun, N.I.; Blom, P.W.M.; Wetzelaer, G.A.H. Electron and hole transport in the organic small molecule  $\alpha$ -NPD. *Appl. Phys. Lett.* **2017**, *110*, 073301. [[CrossRef](#)]
27. Mombrú, D.; Romero, M.; Faccio, R.; Castiglioni, J.; Mombrú, A.W. In situ growth of ceramic quantum dots in polyaniline host via water vapor flow diffusion as potential electrode materials for energy applications. *J. Solid State Chem.* **2017**, *250*, 60–67. [[CrossRef](#)]
28. Mombrú, D.; Romero, M.; Faccio, R.; Mombrú, A.W. Raman and Impedance Spectroscopy under Applied Dc Bias Insights on the Electrical Transport for Donor:Acceptor Nanocomposites Based on Poly(vinyl carbazole) and TiO<sub>2</sub> Quantum Dots. *J. Phys. Chem. C* **2017**, *121*, 23383–23391. [[CrossRef](#)]
29. Mombrú, D.; Romero, M.; Faccio, R.; Tumelero, M.A.; Mombrú, A.W. Extremely Large Magnetic-Field-Effects on the Impedance Response of TiO<sub>2</sub> Quantum Dots. *Sci. Rep.* **2019**, *9*, 5322. [[CrossRef](#)]
30. Hohenberg, P.; Kohn, W. Inhomogeneous Electron Gas. *Phys. Rev.* **1964**, *136*, B864–B871. [[CrossRef](#)]
31. Kohn, W.; Sham, L.J. Self-Consistent Equations Including Exchange and Correlation Effects. *Phys. Rev.* **1965**, *140*, A1133–A1138. [[CrossRef](#)]
32. Kresse, G.; Hafner, J. Ab initio molecular dynamics for liquid metals. *Phys. Rev. B* **1993**, *47*, 558–561. [[CrossRef](#)]
33. Kresse, G.; Hafner, J. Ab initio molecular-dynamics simulation of the liquid-metalamorphous-semiconductor transition in germanium. *Phys. Rev. B* **1994**, *49*, 14251–14269. [[CrossRef](#)]
34. Kresse, G.; Furthmüller, J. Efficient iterative schemes for ab initio total-energy calculations using a plane-wave basis set. *Phys. Rev. B* **1996**, *54*, 11169–11186. [[CrossRef](#)] [[PubMed](#)]
35. Kresse, G.; Furthmüller, J. Efficiency of ab-initio total energy calculations for metals and semiconductors using a plane-wave basis set. *Comput. Mater. Sci.* **1996**, *6*, 15–50. [[CrossRef](#)]
36. Blöchl, P.E. Projector augmented-wave method. *Phys. Rev. B* **1994**, *50*, 17953–17979. [[CrossRef](#)] [[PubMed](#)]
37. Kresse, G.; Joubert, D. From ultrasoft pseudopotentials to the projector augmented wave method. *Phys. Rev. B* **1999**, *59*, 1758–1775. [[CrossRef](#)]
38. Perdew, J.P.; Burke, K.; Ernzerhof, M. Generalized gradient approximation made simple. *Phys. Rev. Lett.* **1996**, *77*, 3865–3868; Erratum in *Phys. Rev. Lett.* **1997**, *78*, 1396. [[CrossRef](#)]
39. Fernández-Werner, L.; Faccio, R.; Juan, A.; Pardo, H.; Montenegro, B.; Mombrú, A.W. Ultrathin (001) and (100) TiO<sub>2</sub>(B) sheets: Surface reactivity and structural properties. *Appl. Surf. Sci.* **2014**, *290*, 180–187. [[CrossRef](#)]
40. Mo, R.; Lei, Z.; Sun, K.; Rooney, D. Facile Synthesis of Anatase TiO<sub>2</sub> Quantum-Dot/Graphene-Nanosheet Composites with Enhanced Electrochemical Performance for Lithium-Ion Batteries. *Adv. Mater.* **2013**, *26*, 2084–2088. [[CrossRef](#)] [[PubMed](#)]
41. Chu, C.W.; Yang, H.; Hou, W.J.; Huang, J.; Li, G.; Yang, Y. Control of the nanoscale crystallinity and phase separation in polymer solar cells. *Appl. Phys. Lett.* **2008**, *92*, 103306. [[CrossRef](#)]
42. Qu, S.; Yao, Q.; Wang, L.; Chen, Z.; Xu, K.; Zeng, H.; Shi, W.; Zhang, T.; Uher, C.; Chen, L. Highly anisotropic P3HT films with enhanced thermoelectric performance via organic small molecule epitaxy. *NPG Asia Mater.* **2016**, *8*, e292. [[CrossRef](#)]
43. Kim, Y.; Cook, S.; Tuladhar, S.M.; Choulis, S.A.; Nelson, J.; Durrant, J.R.; Bradley, D.D.; Giles, M.; McCulloch, I.; Ha, C.S.; et al. A strong regioregularity effect in self-organizing conjugated polymer films and high-efficiency polythiophene:fullerene solar cells. *Nat. Mater.* **2006**, *5*, 197–203. [[CrossRef](#)]
44. Brinkmann, M.J. Structure and morphology control in thin films of regioregular poly (3-hexylthiophene). *Polym. Sci. Part B Polym. Phys.* **2011**, *49*, 1218–1233. [[CrossRef](#)]
45. Singh, R.K.; Kumar, J.; Singh, R.; Kant, R.; Rastogi, R.C.; Chand, S.; Kumar, V. Structure–conductivity correlation in ferric chloride-doped poly (3-hexylthiophene). *New J. Phys.* **2006**, *8*, 112. [[CrossRef](#)]
46. Mombrú, D.; Romero, M.; Faccio, R.; Mombrú, A.W. Roles of amorphous and crystalline regions in determining the optical and electronic properties of donor:acceptor systems comprising poly (3-hexylthiophene) embedded with nitrogen/sulfur-doped graphene quantum dots. *Polym. J.* **2022**, *54*, 1465–1476. [[CrossRef](#)]
47. Wang, W.; Chen, C.; Tollan, C.; Yang, F.; Qin, Y.; Knez, M. Efficient and controllable vapor to solid doping of the polythiophene P3HT by low temperature vapor phase infiltration. *J. Mater. Chem. C* **2017**, *5*, 2686. [[CrossRef](#)]
48. Tsoi, W.C.; James, D.T.; Kim, J.S.; Nicholson, P.G.; Murphy, C.E.; Bradley, D.D.; Nelson, J.; Kim, J.S. The nature of in-plane skeleton Raman modes of P3HT and their correlation to the degree of molecular order in P3HT: PCBM blend thin films. *J. Am. Chem. Soc.* **2011**, *133*, 9834–9843. [[CrossRef](#)]

49. Nightingale, J.; Wade, J.; Moia, D.; Nelson, J.; Kim, J.S. Impact of molecular order on polaron formation in conjugated polymers. *J. Phys. Chem. C* **2018**, *122*, 29129–29140. [[CrossRef](#)]
50. Liang, Z.; Reese, M.O.; Gregg, B.A. Chemically treating poly (3-hexylthiophene) defects to improve bulk heterojunction photovoltaics. *ACS Appl. Mater. Interfaces* **2011**, *3*, 2042–2050. [[CrossRef](#)] [[PubMed](#)]
51. Rahimi, K.; Botiz, I.; Agumba, J.O.; Motamen, S.; Stingelin, N.; Reiter, G. Light absorption of poly (3-hexylthiophene) single crystals. *RSC Adv.* **2014**, *4*, 11121. [[CrossRef](#)]
52. Clark, J.; Silva, C.; Friend, R.H.; Spano, F.C. Role of intermolecular coupling in the photophysics of disordered organic semiconductors: Aggregate emission in regioregular polythiophene. *Phys. Rev. Lett.* **2007**, *98*, 206406. [[CrossRef](#)]
53. Zhang, Y.; Foster, C.W.; Banks, C.E.; Shao, L.; Hou, H.; Zou, G.; Chen, J.; Huang, Z.; Ji, X. Graphene-Rich Wrapped Petal-Like Rutile TiO<sub>2</sub> tuned by Carbon Dots for High-Performance Sodium Storage. *Adv. Mater.* **2016**, *28*, 9391–9399. [[CrossRef](#)]
54. Chiguvare, Z.; Parisi, J. Current conduction in poly (3-Hexylthiophene) and in poly (3-hexylthiophene) doped [6,6]-phenyl C61-butyric acid methylester composite thin film devices. *Z. Naturforsch.* **2012**, *67*, 589–600. [[CrossRef](#)]
55. Mombrú, D.; Romero, M.; Sandoval, M.G.; Faccio, R.; Mombrú, A.W. Role of surface defects on the adsorption of poly(9-vinylcarbazole) on TiO<sub>2</sub> using the monomer as a donor:acceptor model. *Appl. Surf. Sci.* **2019**, *487*, 1104–1110. [[CrossRef](#)]
56. Wong, F.; Perez, G.; Bonilla, M.; Colon-Santana, J.A.; Zhang, X.; Sharma, P.; Gruverman, A.; Dowben, P.A.; Rosa, L.G. Changing molecular band offsets in polymer blends of (P3HT/P(VDF-TrFE)) poly (3-hexylthiophene) and poly (vinylidene fluoride with trifluoroethylene) due to ferroelectric poling. *RSC Adv.* **2014**, *4*, 3020–3027. [[CrossRef](#)]

**Disclaimer/Publisher's Note:** The statements, opinions and data contained in all publications are solely those of the individual author(s) and contributor(s) and not of MDPI and/or the editor(s). MDPI and/or the editor(s) disclaim responsibility for any injury to people or property resulting from any ideas, methods, instructions or products referred to in the content.